JMEPEG (2022) 31:3577–3583
https://doi.org/10.1007/s11665-021-06528-z

1059-9495/$19.00

TECHNICAL ARTICLE

Microstructure and Tensile Property Analysis of 22Cr-3Al Oxide Dispersion Strengthened Steel Obtained Through the STARS Route

Yazhong Zhai, Yingjie Yan, Yongqing Chen, Wei Qin, Hongyan Che, Tiejun Wang, and Rui Cao

Submitted: 30 March 2021 / Revised: 31 October 2021 / Accepted: 26 November 2021 / Published online: 22 January 2022

Oxide dispersion strengthened (ODS) ferritic steels are the candidate structural materials for the advanced nuclear reactors due to their excellent swelling resistance and creep strength. Herein, a 22Cr-3Al ODS steel was prepared through the surface treatment of gas atomized powder, followed by reactive synthesis route and hot isostatic pressing without the mechanical alloying step. As a result, the metastable Fe and Cr oxides formed on the powder surface and promoted the precipitation of Y-Al-O particles at the grain boundaries of the as-hot isostatic pressed steel. In addition, the dispersed oxides with an average size of 97 nm at grain boundaries ensured that the average ultimate tensile strength of the 22Cr-3Al ODS steel is 797 MPa at room temperature.

Keywords ODS steel, oxides, STARS route, tensile properties

1. Introduction

Oxide dispersion strengthened (ODS) ferritic steels are the candidate structural materials for the advanced nuclear reactors because of their high strength at high temperatures, excellent creep resistance (Ref 1-5), and radiation tolerance (Ref 6). In addition to the fine microstructure, the superior performance of ODS ferritic steels is also attributed to the fine and dispersed stable oxide particles. Moreover, oxide dispersion strengthening plays a vital role in improving the performance of the ODS steels (Ref 7-9). Notably, the dispersed oxides mainly belong to yttrium and titanium, including Y_2O_3 and Y-Ti-O ($Y_2Ti_2O_7$, $YTiO_3$, and Y_2TiO_5) (Ref 10-13), which have high stability and a low coarsening rate at high temperatures (Ref 14).

Mechanical alloying (MA) is the most common method of introducing the dispersed oxides in ODS steel. During the MA process, the pre-alloyed powders are milled with yttrium oxide particles using a high-energy ball to ensure that the particles are crushed and form a solid solution in the matrix (Ref 15). Following this, the Y-containing powders are consolidated through hot isostatic pressing (HIP) or hot extrusion to obtain fully dense materials. During the consolidation process, the stable nano-oxides precipitated at the matrix. In addition, adjusting the parameters of ball milling (Ref 16) and introducing the reactive elements can further reduce the size of the nano-oxides (Ref 17, 18). However, some inherent drawbacks of MA, like long durations, a high cost, and contamination from the jars or atmosphere, limit the large-scale application of ODS steel in the industry.

The Surface Treatment of gas Atomized powder followed by the Reactive Synthesis (STARS) route is a way to produce ODS alloys without the MA. In the STARS route, the Y-containing powders were produced by gas atomization firstly and the as-atomized powders were then oxidized in the air with suitable temperature and time, which avoided the MA step to introduce yttrium and oxygen in the pre-alloyed powders. The STARS route can effectively improve the purity and uniformity of the powders (Ref 19-21) and shorten the time of preparing the pre-alloyed powders. Notably, there are some differences in the microstructure and properties of the ODS steels produced with and without MA. ODS alloys produced via MA possessed finer microstructure, higher density dislocations and dispersive nano-oxides. The ultimate tensile strength (UTS) of the 14YWT produced with the MA process could be up to 1.2 GPa at room temperature (Ref 7), while through the STARS route, the UTS was merely about 500 MPa (Ref 22). Similarly, the UTS of the ODS PM2000 with higher Cr and Al content produced via SLM is about 500 MPa as well (Ref 23, 24). Big grain size is one reason for the low strength of the ODS steels produced by STARS and SLM. So decreasing the diameter of gas-atomized powders and refining grain of alloy by thermal mechanical treatment (TMT) are operative approaches to improve the properties of the ODS alloys produced through the STARS route via optimizing the microstructure.

In the present study, the 22Cr-3Al-0.4Y powders were produced through the STARS processing route and then consolidated through the HIP. The oxides on the powder surface after the STARS process and the precipitates in the as-HIPed steel were characterized in detail. In addition, the tensile properties and fracture mechanisms of the as-HIPed alloy were

Yazhong Zhai, Yingjie Yan, Yongqing Chen, and **Rui Cao**, State Key Laboratory of Advanced Processing and Recycling of Nonferrous Metals, Lanzhou University of Technology, Qilihe District, Langongping 287 roadGansu province, Lanzhou 730050, China; and School of Materials Science and Engineering, Lanzhou University of Technology, Lanzhou 730050 Gansu, China; and **Wei Qin, Hongyan Che,** and **Tiejun Wang**, Advanced Technology & Materials Limited Company, Iron & Steel Research Institute Group, Beijing 100081, China. Contact e-mail: yjyan@lut.edu.cn.

investigated at different temperatures. Moreover, the effects of powder surface oxides on the precipitates and tensile properties of 22Cr-3Al ODS steel were discussed.

2. Material and Methods

The powders produced through Ar-gas-atomization were mainly spherical, with a mean size of about 6.5 μm. The gas-atomized powders were then oxidized at 400 °C for 24 hours in the muffle furnace to form the metastable oxides on the powder surfaces. Following this, the powders were consolidated through HIP under a pressure of 150 MPa at 1100 °C for 2 hours. The chemical composition of the as-HIPed alloy is shown in Table 1.

Moreover, the oxides on the powder surfaces were analyzed through X-ray photoelectron spectroscopy (XPS) in a Kratos AXIS SUPRA using a monochromatic source of X-ray Al Kα (1486.6 eV). The microstructure and distribution of precipitates in the as-HIPed alloy were then investigated using the scanning electron microscope (SEM, Quanta 450FEG) and transmission electron microscopy (TEM, JEM-2100F). Notably, the foil samples were mechanically thinned to 60 μm and a diameter of 3 mm, for TEM analysis. Thereafter, the thin foils were electropolished using an MTA-1A twin jet polisher with a solution of 10% perchloric acid + 90% alcohol at −30 °C. The tensile tests were carried out with a strain rate of 1 mm/min at 25, 500, and 1000 °C, respectively. Finally, the fracture surfaces of the tensile samples were observed through SEM.

3. Results

3.1 Microstructure of the powders

Figure 1(a) and (b) shows the morphology of the oxidized powders. These powders are mainly spherical. Numerous precipitates were observed on the powder surface, part of them was pointed by white arrows, as shown in Fig. 1(c) (high magnification of the area inside the dashed red line in (b)). The size of oxide particles on the powder surface is too small to exceed the resolution of SEM, which is difficult to count the size of the oxide particles.

3.2 XPS Results of Oxides on the Powder Surfaces

The XPS results of the oxidized powders are shown in Figs. 2 and 3. The XPS survey spectra in Fig. 2 revealed the presence of Fe, Y, Al, W, Cr, Mn, O, and C elements on the surface of the powders. Figure 3 shows the detailed high-resolution spectra of Fe, Cr, Al, O, and Y. Notably, the Fe element on the powder surfaces was partially oxidized (Fig. 3a), and the Fe-oxide layers were mainly composed of Fe_2O_3 (Fe^{3+}) and FeO (Fe^{2+}). The Cr element on the powder surfaces mainly appeared in the form of chromium oxide (Cr^{ox}, $2p_{3/2}$ and $2p_{1/2}$ peak positions at 575.8 eV and 586 eV, respectively), as shown in Fig. 3(b). Combined with the O 1s spectrum in Fig. 3(a) and (d), oxygen existed in two states and these contributed to the formation of metallic oxides (O2-, 529.7 eV) and hydroxyl groups (OH-, 531.2 eV). Additionally, the peak pairs with binding energies of about 156.8 eV and 158.8 eV observed in Fig. 3(e) corresponded to Y $3d_{5/2}$ and Y $3d_{3/2}$ (Ref 25), indicating that the Y element on the powder surfaces mainly existed as Y-rich oxides.

Table 1 Chemical composition of the 22Cr-3Al ODS steel (wt.%)

Materials	Cr	Al	Y	O	Mn	Zr	Ti	Fe
Fe-22Cr-3Al	22.48	2.67	0.4	0.28	0.34	0.06	0.06	Bal

3.3 Microstructure of the as-HIPed Steel

Figure 4 shows the microstructures of the as-HIPed samples. SEM micrographs of the microstructure are shown in Fig. 4(a), and the average grain size was 6.3 μm as shown by the statistical result in Fig. 4(b). Dispersed precipitates were observed in the matrix and were highlighted by the white arrows in Fig. 4(c). In addition, the precipitates were mainly located at the grain boundaries, and part of the precipitates

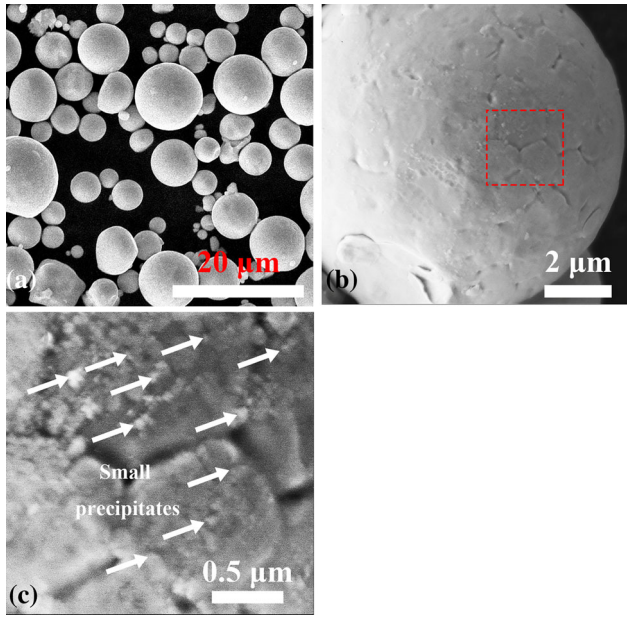

Fig. 1 SEM image of the STARSed powder. (a) Macro-morphology and (b) micro-morphology of the powder; (c) high magnification of the area inside the dashed red line in (b) (Color figure online)

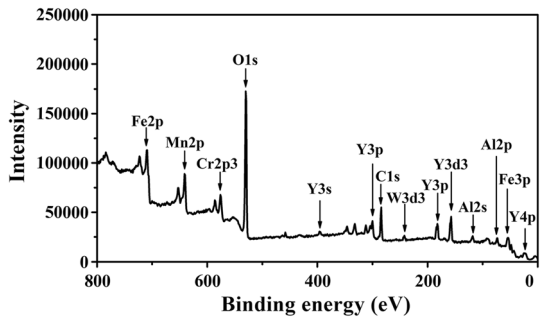

Fig. 2 XPS survey spectra of the as-atomized powders after oxidation at 400 °C

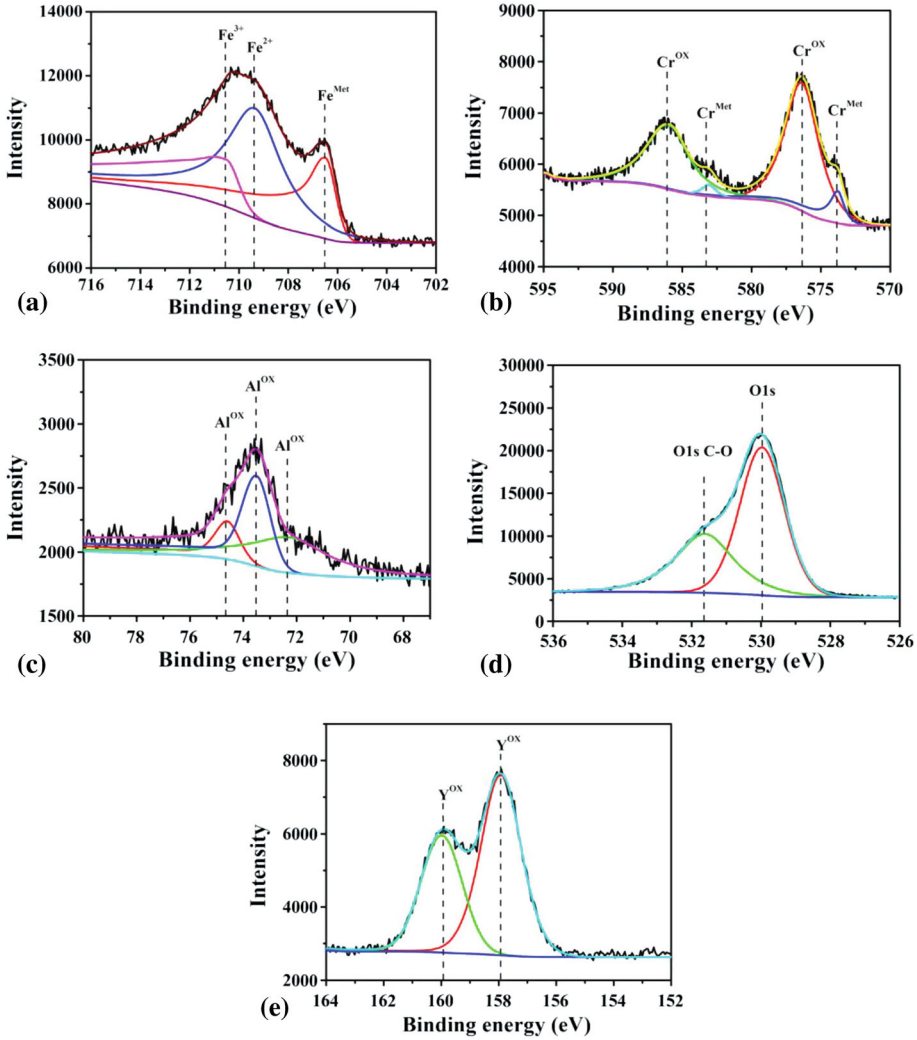

Fig. 3 Detailed XPS spectra of Fe, Cr, Al, O and Y on the surface of the as-atomized powders after oxidation at 400 °C

locates inside grains. The statistical results showed that those precipitates had an average diameter of about 97 nm (Fig. 4d). Figure 4(e) shows the TEM micrographs of the precipitates at grain boundaries. The EDS results of the precipitates (pointed by white arrows) are shown in Fig. 4(f). The results showed that the precipitates were mainly (Y, Al)-containing oxides. The presence of Zr/Ti-rich oxides in Fig. 4(e) may be the elements segregation within the individual powder.

3.4 Tensile Properties and Fracture Surfaces

Figure 5 shows the ultimate tensile strength (UTS), the yield strength (YS), and elongation of the as-HIPed alloy, tested at 25, 500, and 1000 °C. Notably, the average UTS, YS, and elongation of the alloy at 25 °C were 797 MPa, 669 MPa, and 9%, respectively. With the test temperature raised to 500 °C, the average UTS and YS decreased to 536 and 425 MPa, respectively, and the average elongation of the alloy increased to 24%. Moreover, when the test temperature up to 1000 °C, the average UTS, YS, and elongation of the alloy were 50 MPa, 26 MPa, and 43%, respectively.

Figure 6 shows fractography of the as-HIPed samples tested at 25, 500, 1000 °C. Figure 6(a) shows the macro-morphology of the fracture at 25 °C, as can be seen, the fracture surface is relatively flat. Micro-image (Fig. 6b) of the sample displayed a dimpled and cleavage fracture morphology on the fracture surface. The cleavage steps on the fracture surface are also highlighted by the red arrows in Fig. 6(b). At higher temperatures (500 and 1000 °C), the samples underwent more deformation before fracture and the fracture mode changed to ductility mode as shown in Fig. 6(c) and (e). More depth dimples were found on the fracture surfaces when the test temperature increased to 500 °C (Fig. 6d) and 1000 °C (Fig. 6f) and the precipitates presented in the dimples.

4. Discussion

4.1 Effect of Powder Surface Oxide on the Precipitates

In the present study, various metal oxides formed on the surface of the powders after oxidation treatment at 400 °C, as shown in Fig. 3. The metastable Fe_2O_3 and Cr_2O_3 and stable Y_2O_3 and γ-Al_2O_3 oxides (Ref 26) formed on the powder surface. As the reports of D. Pazos (Ref 22) and E. Gil (Ref 20, 27), the oxide layer of metastable Fe_2O_3 and Cr_2O_3 on the powder surface was about 60 nm, and the Al- and Y-rich

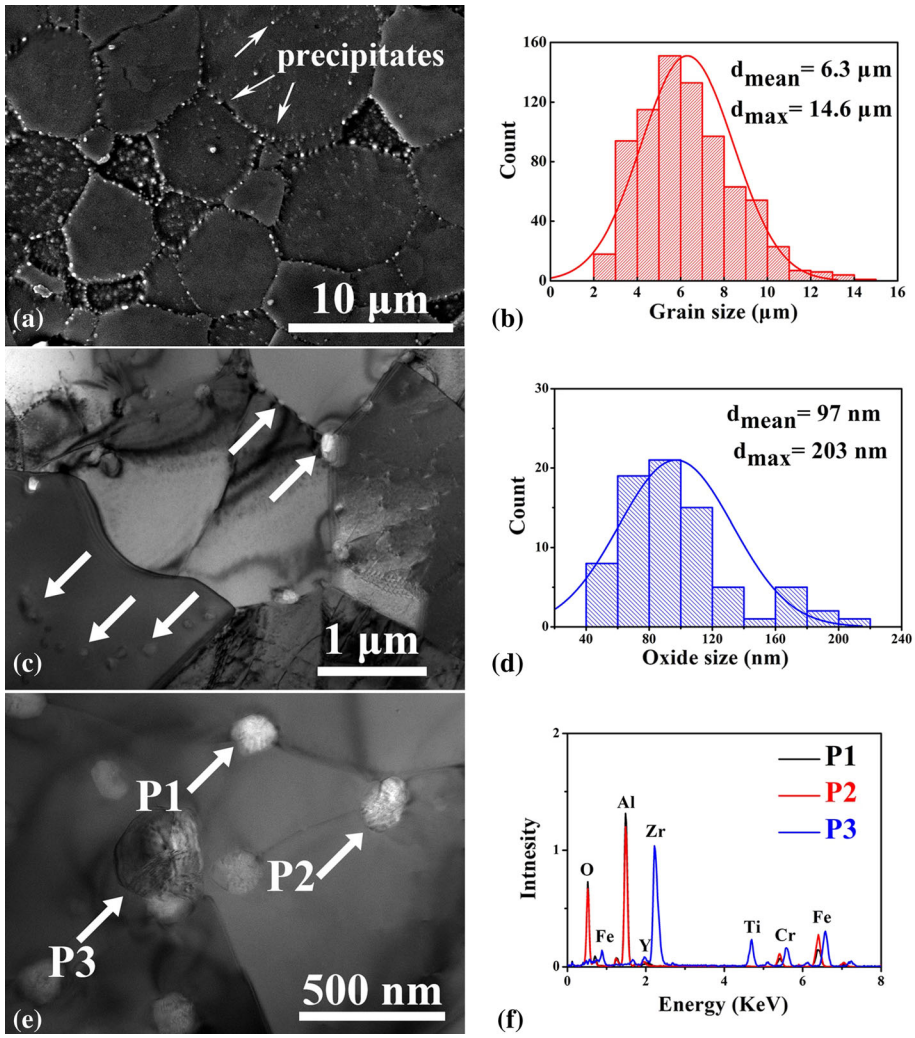

Fig. 4 Microstructure of the 22Cr-3Al ODS steel: (a) SEM image and (b) distribution of grain size of the steel; (c) TEM macro-image of the precipitates at the grain boundaries and inside grains; (d) distribution of oxide size in alloys; (e) TEM micro-image of the precipitates at grain boundaries; (f) EDS results of the precipitates pointed by white arrows in (e)

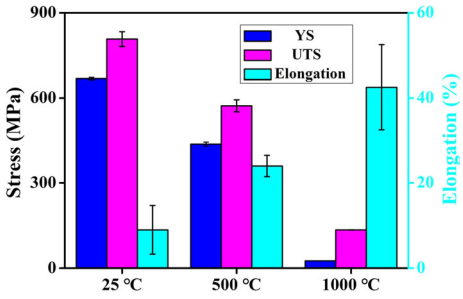

Fig. 5 Ultimate tensile strength (UTS), yield strength (YS) and elongation of the 22Cr-3Al ODS steel at 25, 500 and 1000 °C

oxides preferentially appeared at the grain boundaries as the isolated particles.

During the HIP process, the metastable Fe- and Cr-oxides decomposed (Ref 27), and the Y and Al oxides remained due to their high thermal stability. The oxygen from the decomposed metastable oxides is available and diffuse inside grains. It can react with Al and Y to form thermodynamically stable α-Al_2O_3 and Y_2O_3 oxides within the matrix. Besides, the Al_2O_3 could directly react with Y_2O_3 to form Y-Al-O oxides ($YAlO_3$, $Y_3Al_5O_{12}$, and $Y_4A_{l2}O_9$) (Ref 28, 29). Because selected area electron diffraction was not conducted to further analysis the type of oxides, these oxides shown in Fig. 4(e) and (f) were collectively referred to as (Y, Al)-containing oxides. These stable nano-oxides can pin the grain boundaries and suppress the growth of grains.

4.2 Effect of Microstructure on Tensile Properties

The strength of ODS steel is affected by many factors, and the following Eq 1 is usually used to predict the strength of the ODS steel (Ref 30):

$$\sigma_y = \sigma_0 + \sigma_{ss} + \sigma_{gb} + \sqrt{\sigma_{dis}^2 + \sigma_p^2} \quad \text{(Eq 1)}$$

where σ_y represents the yield strength of ODS steel, σ_0 represents the friction stress of pure iron, σ_{ss} and σ_{gb} represent the solid solution strengthening and grain boundary strengthening, σ_{dis} and σ_p represent the dislocation strengthening and oxide dispersion strengthening, respectively. The alloy with smaller grain sizes, smaller and dispersed oxides could possess higher yield stress. Due to the low HIP temperature and the

precipitation of nano-oxides, the small size of the grains was inherited and not coarse during the HIP process. Thus, the 22Cr-3Al ODS steel has a uniform and fine microstructure, and the average size of grain and oxides was 6.3 μm and 97 nm, which are smaller than that of the 14Cr-2W ODS alloy (Ref 22) and the PM2000 alloy (Ref 7). In addition, PPBs formed within the 14Cr-2W ODS alloys produced the STARS route (Ref 22), and poly-crystalline and coarsen oxides formed within the PM2000 alloy. Thus, the 22Cr-3Al alloy possesses higher strength compared to that of the 14Cr-2W (Ref 22) and the PM2000 (Ref 7), while maintaining a similar strength to the APMT alloy (Ref 31), as shown in Fig. 7. There are small error bars of mechanical strength at different temperatures, as shown in Fig. 5. Compared to the 14YWT alloys produced through MA (Ref 7) with grain size about a few hundred nanometers and oxide diameter about 10 nm, the 22Cr-3Al alloy possessed coarser grain and oxides. Thus, the UTS of 14YWT (about 1253 MPa) (Ref 7) is higher than the UTS of 22Cr-3Al alloy.

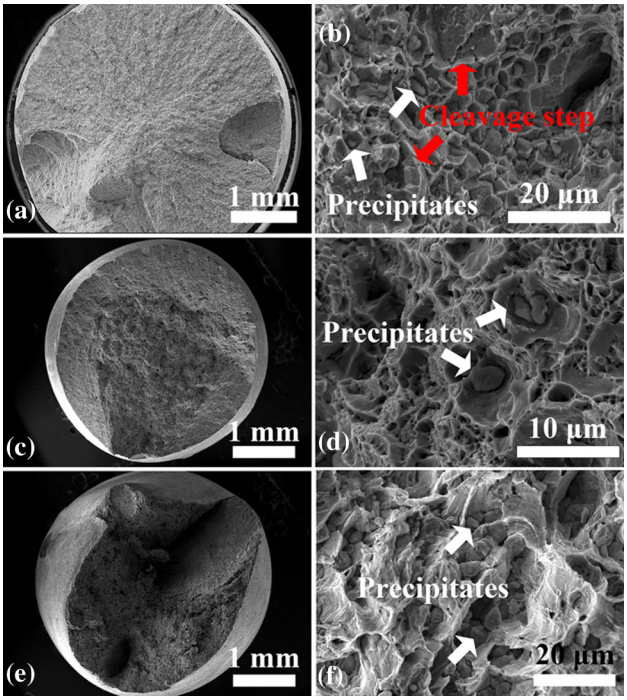

Fig. 6 SEM images of the fracture surface of the tensile tested samples at 25 , 500, 1000 °C, respectively: (a, b) macro- and micro-morphology of the brittle fracture of an as-HIPed sample tested at 25 °C. The cleavage steps are indicated by write arrows; (c), (d) macro- and micro-morphology of the dimple fracture surface of an as-HIPed sample tested at 500 °C. Precipitates are pointed by white arrows; (e, f) macro- and micro-morphology of the fracture of an as-HIPed sample tested at 1000 °C. Precipitates are pointed by white arrows

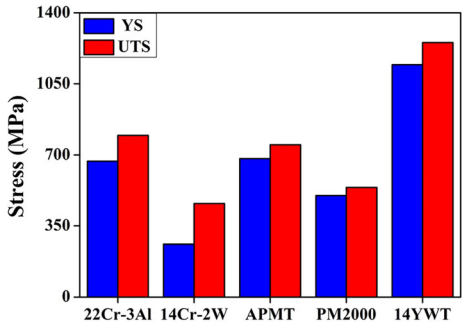

Fig. 7 Comparison of mechanical properties at room temperature of ODS steels prepared by different compositions and processes (Ref 7, 22, 23, 31)

The high content of Cr and Al, and the big precipitates at the grain boundaries are the main reasons for the low elongation of the 22Cr-3Al ODS steel (only 9% at room temperature) (Ref 32-36). The oxide particles were found on the fracture surface, as shown in Fig. 6(b). Under the applied load, the difference in stiffness of the matrix and oxide particles leads to the initiation and propagation of microcracks along with the interfaces of them, eventually occur brittle fracture of the alloy (Ref 36).

The strength of the 22Cr-3Al ODS steel decreased with temperature up. When tested temperatures increased from 25 to 1000 °C, the UTS of the steel decreased from 797 to 50 MPa. The fracture mode changed from cleavage fracture to ductility fracture, and there are more small dimples on the fracture surfaces tested at elevated temperatures as shown in Fig. 6(d) and (f). When the tested temperature was above 700 °C, the contribution of solution strengthening, fine grain strengthening, and dislocation strengthening decreased (Ref 37, 38). The dispersed and stable oxides become the key to improve the elevated-temperature strength by hindering boundary movement (Ref 3, 31, 39-41). In the 22Cr-3Al ODS steel, the intragranular Al-containing oxides could cause the Orowan strengthening effect (Ref 29, 38, 42, 43), and the oxides at grain boundaries could effectively inhibit grain boundary movement and grain coarsening. So the steel still had a certain strength at elevated temperatures.

Compared to the ODS steel produced through MA (Ref 7, 24, 26, 27), the grain size of the 22Cr-3Al ODS steel in the present study was large (about 6.3 μm), and the precipitates within the grain were less. Both of these significantly affect the performance of the steel. Also, suitable thermal mechanical treatment process may improve the mechanical properties of the 22Cr-3Al ODS steel via optimizing the grain size and dispersing the grain boundaries precipitates (Ref 44, 45).

5. Conclusion

The study successfully prepared the 22Cr-3Al ODS steel through the STARS and HIP processes. In addition, the microstructure and tensile properties of the 22Cr-3Al ODS steel were investigated in detail. Consequently, two main conclusions were drawn:

(1) Fe-, Cr-, Al- and Y-oxides were present on the surfaces of powders produced through STARS route. After the HIP process, the stable (Y, Al)-containing oxides precipitated at the grain boundaries and the average grain size was 6.3 μm.

(2) The average ultimate tensile strength and elongation of as-HIPed alloy were 797 MPa and 9%, respectively, at 25 °C. However, the average ultimate tensile strength decreased to 536 MPa, while average elongation increased to 24% with a dimple fracture, when the temperature increased to 500 °C. Moreover, the average ultimate tensile strength and elongation were 50 MPa and 43%, respectively, at 1000 °C.

Acknowledgment

This work was supported by the National Natural Science Foundation of China (51961024, 52071170, 51761027).

Data Availability

The raw/processed data required to reproduce these findings cannot be shared at this time as the data also form part of an ongoing study.

Reference

1. E. Aydogan, J.S. Weaver, U. Carvajal-Nunez, M.M. Schneider, J.G. Gigax, D.L. Krumwiede, P. Hosemann, T.A. Saleh, N.A. Mara, D.T. Hoelzer, B. Hilton and S.A. Maloy, Response of 14YWT Alloys Under Neutron Irradiation: A Complementary Study on Microstructure and Mechanical Properties, *Acta Mater.*, 2019, **167**, p 181–196.
2. M.C. Brandes, L. Kovarik, M.K. Miller, G.S. Daehn and M.J. Mills, Creep Behavior and Deformation Mechanisms in a Nanocluster Strengthened Ferritic Steel, *Acta Mater.*, 2012, **60**(4), p 1827–1839.
3. T. Hayashi, P.M. Sarosi, J.H. Schneibel and M.J. Mills, Creep Response and Deformation Processes in Nanocluster-Strengthened Ferritic Steels, *Acta Mater.*, 2008, **56**(7), p 1407–1416.
4. P.V. Durga, K.S. Prasad, S.B. Chandrasekhar, A.V. Reddy, S.R. Bakshi and R. Vijay, Microstructural and Mechanical Properties of Oxide Dispersion Strengthened Iron Aluminides Produced by Mechanical Milling and Hot Extrusion, *J. Alloy. Compd.*, 2020, **834**, p 155218–155223.
5. Y.Y. Peng, L.M. Yu, Y.C. Liu, Z.Q. Ma, C.X. Liu, C. Li and H.J. Li, Effect of Ageing Treatment at 650 °C on Microstructure and Properties of 9Cr-ODS Steel, *Acta Metall. Sin*, 2020, **56**(8), p 1075–1083.
6. T. Stan, Y. Wu, J. Ciston, T. Yamamoto and G.R. Odette, Characterization of Polyhedral Nano-Oxides and Helium Bubbles in an Annealed Nanostructured Ferritic Alloy, *Acta Mater.*, 2020, **183**, p 484–492.
7. M.E. Alam, S. Pal, K. Fields, S.A. Maloy, D.T. Hoelzer and G.R. Odette, Tensile Deformation and Fracture Properties of a 14YWT Nanostructured Ferritic Alloy, *Mater. Sci. Eng., A*, 2016, **675**, p 437–448.
8. E. Aydogan, O. El-Atwani, S. Takajo, S.C. Vogel and S.A. Maloy, High Temperature Microstructural Stability and Recrystallization Mechanisms in 14YWT Alloys, *Acta Mater.*, 2018, **148**, p 467–481.
9. A. Hirata, T. Fujita, C.T. Liu and M.W. Chen, Characterization of Oxide Nanoprecipitates in an Oxide Dispersion Strengthened 14YWT Steel Using Aberration-Corrected STEM, *Acta Mater.*, 2012, **60**(16), p 5686–5696.
10. A.J. London, S. Santra, S. Amirthapandian, B.K. Panigrahi, R.M. Sarguna, S. Balaji, R. Vijay, C.S. Sundar, S. Lozano-Perez and C.R.M. Grovenor, Effect of Ti and Cr on Dispersion, Structure and Composition of Oxide Nano-Particles in Model ODS Alloys, *Acta Mater.*, 2015, **97**, p 223–233.
11. J. Ribis and Y. de Carlan, Interfacial Strained Structure and Orientation Relationships of the Nanosized Oxide Particles Deduced from Elasticity-Driven Morphology in Oxide Dispersion Strengthened Materials, *Acta Mater.*, 2012, **60**(1), p 238–252.
12. Y. Wu, J. Ciston, S. Kräemer, N. Bailey, G.R. Odette and P. Hosemann, The Crystal Structure, Orientation Relationships and Interfaces of the Nanoscale Oxides in Nanostructured Ferritic Alloys, *Acta Mater.*, 2016, **111**, p 108–115.
13. T. Gadipelly, A. Dasgupta, C. Ghosh, V. Krupa, D. Sornadurai, B.K. Sahu and S. Dhara, Synthesis and Structural Characterisation of Y2Ti2O7 using Microwave Hydrothermal Route, *J. Alloy. Compd.*, 2020, **814**, p 152273–152280.
14. C.P. Massey, S.N. Dryepondt, P.D. Edmondson, M.G. Frith, K.C. Littrell, A. Kini, B. Gault, K.A. Terrani and S.J. Zinkle, Multiscale Investigations of Nanoprecipitate Nucleation, Growth, and Coarsening in Annealed Low-Cr Oxide Dispersion Strengthened FeCrAl Powder, *Acta Mater.*, 2019, **166**, p 1–17.
15. M. Dadé, J. Malaplate, J. Garnier, F. De Geuser, F. Barcelo, P. Wident and A. Deschamps, Influence of Microstructural Parameters on the Mechanical Properties of Oxide Dispersion Strengthened Fe-14Cr Steels, *Acta Mater.*, 2017, **127**, p 165–177.
16. M.J. Alinger, G.R. Odette and D.T. Hoelzer, On the Role of Alloy Composition and Processing Parameters in Nanocluster Formation and Dispersion Strengthening in Nanostuctured Ferritic Alloys, *Acta Mater.*, 2009, **57**(2), p 392–406.
17. L. Zhang, L. Yu, Y. Liu, C. Liu, H. Li and J. Wu, Influence of Zr Addition on the Microstructures and Mechanical Properties of 14Cr ODS Steels, *Mater. Sci. Eng., A*, 2017, **695**, p 66–73.
18. E. Wessel, V. Kochubey, D. Naumenko, L. Niewolak, L. Singheiser and W.J. Quadakkers, Effect of Zr Addition on the Microstructure of the Alumina Scales on FeCrAlY-Alloys, *Scripta Mater.*, 2004, **51**(10), p 987–992.
19. J.R. Rieken, I.E. Anderson, M.J. Kramer, G.R. Odette, E. Stergar and E. Haney, Reactive Gas Atomization Processing for Fe-Based ODS Alloys, *J. Nucl. Mater.*, 2012, **428**(1–3), p 65–75.
20. E. Gil, J. Cortés, I. Iturriza and N. Ordás, XPS and SEM Analysis of the Surface of Gas Atomized Powder Precursor of ODS Ferritic Steels Obtained Through the STARS Route, *Appl. Surf. Sci.*, 2018, **427**, p 182–191.
21. E. Gil, N. Ordás, C. García-Rosales and I. Iturriza, Microstructural Characterization of ODS Ferritic Steels at Different Processing Stages, *Fusion Eng. Des.*, 2015, **98–99**, p 1973–1977.
22. D. Pazos, A. Cintins, V. de Castro, P. Fernández, J. Hoffmann, W.G. Vargas, T. Leguey, J. Purans, A. Anspoks, A. Kuzmin, I. Iturriza and N. Ordás, ODS Ferritic Steels Obtained from Gas Atomized Powders Through the STARS Processing Route: Reactive Synthesis as an Alternative to Mechanical Alloying, *Nuclear Mater. Energy*, 2018, **17**, p 1–8.
23. T. Boegelein, S.N. Dryepondt, A. Pandey, K. Dawson and G.J. Tatlock, Mechanical Response and Deformation Mechanisms of Ferritic Oxide Dispersion Strengthened Steel Structures Produced by Selective Laser Melting, *Acta Mater.*, 2015, **87**, p 201–215.
24. Y.N. Shi, Z. Lu, L. Yu, R. Xie, Y.H. Ren and G. Yang, Microstructure and Tensile Properties of Zr-Containing ODS-FeCrAl Alloy Fabricated by Laser Additive Manufacturing, *Mat Sci Eng a-Struct*, 2020, **774**, p 138937–138947.
25. S.A. Barve, M.N. Deo, R. Kishore, A. Biswas, L.M. Gantayet and D.S. Patil, Effect of Argon Ion Activity on the Properties of Y2O3 Thin Films Deposited by Low Pressure PACVD, *Appl. Surf. Sci.*, 2010, **257**(1), p 215–221.
26. Q. Zhao, L. Yu, Y. Liu, Y. Huang, Q. Guo, H. Li and J. Wu, Evolution of Al-Containing Phases in ODS Steel by Hot Pressing and Annealing, *Powder Technol.*, 2017, **311**, p 449–455.
27. N. Ordás, E. Gil, A. Cintins, V. de Castro, T. Leguey, I. Iturriza, J. Purans, A. Anspoks, A. Kuzmin and A. Kalinko, The Role of Yttrium and Titanium During the Development of ODS Ferritic Steels Obtained Through the STARS Route: TEM and XAS Study, *J. Nucl. Mater.*, 2018, **504**, p 8–22.
28. G. Zhang, Z. Zhou, K. Mo, P. Wang, Y. Miao, S. Li, M. Wang, X. Liu, M. Gong, J. Almer and J.F. Stubbins, The Microstructure and Mechanical Properties of Al-Containing 9Cr ODS Ferritic Alloy, *J. Alloy. Compd.*, 2015, **648**, p 223–228.
29. S. Xu, Z. Zhou, F. Long, H. Jia, N. Guo, Z. Yao and M.R. Daymond, Combination of Back Stress Strengthening and Orowan Strengthening in Bimodal Structured Fe–9Cr–Al ODS Steel with High Al Addition, *Mater. Sci. Eng., A*, 2019, **739**, p 45–52.
30. X. Zhou, Y. Liu, L. Yu, Z. Ma, Q. Guo, Y. Huang and H. Li, Microstructure Characteristic and Mechanical Property of Transformable 9Cr-ODS Steel Fabricated by Spark Plasma Sintering, *Mater. Des.*, 2017, **132**, p 158–169.
31. A. Guria, I. Charit, B. Petrovic, Tensile Deformation Behavior of Al-rich Ferritic Steels for Advanced Light Water Reactors. *Frontiers in Materials Processing, Applications, Research and Technology*, M. Muruganant, A. Chirazi, B. Raj, Eds., Springer, 2018, p 35–45
32. J.H. Lee, Development of Oxide Dispersion Strengthened Ferritic Steels with and Without Aluminum, *Front. Energy*, 2012, **6**(1), p 29–34.
33. J.H. Lee and J.H. Kim, Characterization of Oxide Nanoparticles in Al-Free and Al-Containing Oxide Dispersion Strengthened Ferritic Steels, *J. Nanosci. Nanotechnol.*, 2013, **13**(9), p 6169–6173.

34. G. Liu, G.J. Zhang, F. Jiang, X.D. Ding, Y.J. Sun, J. Sun and E. Ma, Nanostructured High-Strength Molybdenum Alloys with Unprecedented Tensile Ductility, *Nat Mater*, 2013, **12**(4), p 344–350.
35. L. Ma, S. Hu, J. Shen, J. Han and Z. Zhu, Effects of Cr Content on the Microstructure and Properties of 26Cr–3.5Mo–2Ni and 29Cr–3.5Mo–2Ni Super Ferritic Stainless Steels, *J. Mater. Sci. Technol.*, 2016, **32**(6), p 552–560.
36. S. Li, Z. Zhou, J. Jang, M. Wang, H. Hu, H. Sun, L. Zou, G. Zhang and L. Zhang, The Influence of Cr Content on the Mechanical Properties of ODS Ferritic Steels, *J. Nucl. Mater.*, 2014, **455**(1–3), p 194–200.
37. U. Zerbst, M. Madia, C. Klinger, D. Bettge and Y. Murakami, Defects as a Root Cause of Fatigue Failure of Metallic Components II: Non-Metallic Inclusions, *Eng. Fail. Anal.*, 2019, **98**, p 228–239.
38. J.H. Kim, T.S. Byun, D.T. Hoelzer, S.W. Kim and B.H. Lee, Temperature Dependence of Strengthening Mechanisms in the Nanostructured Ferritic Alloy 14YWT: Part I—Mechanical and Microstructural Observations, *Mater. Sci. Eng., A*, 2013, **559**, p 101–110.
39. X. Boulnat, N. Sallez, M. Dadé, A. Borbély, J.L. Béchade, Y. de Carlan, J. Malaplate, Y. Bréchet, F. de Geuser, A. Deschamps, P. Donnadieu, D. Fabrègue and M. Perez, Influence of Oxide Volume Fraction on Abnormal Growth of Nanostructured Ferritic Steels During Non-Isothermal Treatments: An In Situ Study, *Acta Mater.*, 2015, **97**, p 124–130.
40. S. Ma, A. Li, S. Zhou, Y. Yang, S. Wang and M. Liu, Microstructure and Mechanical Properties of Nickel Strengthened by Y2O3 Through Rock-Milling and Spark Plasma Sintering, *J. Alloy. Compd.*, 2018, **750**, p 911–916.
41. K. Kallip, N.K. Babu, K.A. AlOgab, L. Kollo, X. Maeder, Y. Arroyo and M. Leparoux, Microstructure and Mechanical Properties of Near Net Shaped Aluminium/Alumina Nanocomposites Fabricated by Powder Metallurgy, *J. Alloy. Compd.*, 2017, **714**, p 133–143.
42. J.F. Nie, Effects of Precipitate Shape and Orientation on Dispersion Strengthening in Magnesium Alloys, *Scripta Mater.*, 2003, **48**(8), p 1009–1015.
43. K.M. Sree Manu, S. Arun Kumar, T.P.D. Rajan, M. Riyas Mohammed and B.C. Pai, Effect of Alumina Nanoparticle on Strengthening of Al-Si Alloy Through Dendrite Refinement, Interfacial Bonding and Dislocation Bowing, *J. Alloys Comp.*, 2017, **712**, p 394–405.
44. J. Macías-Delgado, T. Leguey and V. de Castro, Effect of Hot Cross Rolling on the Microstructure and Mechanical Properties of an Fe-14Cr ODS ferritic steel, *Mater. Sci. Eng., A*, 2018, **711**, p 448–459.
45. H.-L. Yu, X.-H. Liu, H.-Y. Bi and L.-Q. Chen, Deformation Behavior of Inclusions in Stainless Steel Strips During Multi-Pass Cold Rolling, *J. Mater. Process. Technol.*, 2009, **209**(1), p 455–461.